catalysts

MDPI

Article

Development of $SrTiO_3$ Photocatalysts with Visible Light Response Using Amino Acids as Dopant Sources for the Degradation of Organic Pollutants in Aqueous Systems

Panagiotis-Spyridon Konstas, Ioannis Konstantinou *, Dimitrios Petrakis and Triantafyllos Albanis *

Department of Chemistry, University of Ioannina, 45110 Ioannina, Greece; pkonstas@cc.uoi.gr (P.-S.K.); dpetrakis@uoi.gr (D.P.)

* Correspondence: iokonst@cc.uoi.gr (I.K.); talbanis@uoi.gr (T.A.); Tel.: +30-265-100-8349 (I.K.); +30-265-100-8348 (T.A.)

Received: 16 October 2018; Accepted: 2 November 2018; Published: 8 November 2018

Abstract: N-doped and N,S-co-doped $SrTiO_3$ photocatalysts were prepared using glycine and L-histidine amino acids as nitrogen sources and L-cysteine as nitrogen and sulphur source. The samples were characterized by X-ray diffraction (XRD), scanning electron microscopy (SEM), N_2 porosimetry, UV-Vis diffuse reflectance (DRS) and fluorescence spectroscopy, dynamic light scattering (DLS). Cubic $SrTiO_3$ phase is formed in all samples, with crystal size ranged from 14.2 nm to 35.7 nm. The catalysts' specific surface area and porosity depend on the amino acid dopant showing micro-mesoporosity for glycine, mesoporosity for histidine and non-porosity for cysteine. The lowest band gap (2.95 eV) was observed for the sample G-N-STO3 prepared with glycine (N:Sr:Ti 3:1:1 molar ratio) which produced also the higher amount of $^{\bullet}OH$ radicals. The photocatalytic activity was tested against the degradation of methylene blue (MB) dye under UV-Vis and visible light irradiation following first-order kinetics.

Keywords: N-doping; perovskites; $SrTiO_3$; photocatalysis; amino acids

1. Introduction

Simple perovskite—type oxides with the general formula ABO_3, where A is an alkaline earth metal, or a rare material and B is a transition metal from the first raw of the periodic table have received wide technological applications including catalytic and photocatalytic processes [1–4]. Among them, titanate perovskites $ATiO_3$ (A = Ca, Sr, Ba, etc.) are semiconductor materials with a wide band gap and intriguing electronic, optical, magnetic and photocatalytic properties. They constitute promising materials for photocatalytic processes due to their resistance to photo corrosion and their high physicochemical stability [5–8]. $SrTiO_3$ (STO) is among the most promising simple titanate perovkite for photocatalytic applications [9–12]. It is a cubic perovskite (Pm3m, a = 3.9 Å) n-type semiconductor with an indirect band gap of 3.1–3.7 eV depending on the crystal structure and morphology obtained by the synthesis method followed [13,14].

This band gap energy renders $SrTiO_3$ an excellent photocatalyst only under UV light, including about 5.0% of sunlight energy [15]. As a result the modification of $SrTiO_3$ to increase absorptivity into the visible light spectrum has been assayed mainly via transition metal doping of the Ti site with metals like Mn, Ru, Cr, Rh, Ru and Ir [10,16–20] or deposition of noble metals like Au and Pt on the semiconductor surface [16,21]. However, the use of rare or precious metals, the formation of other phases as well as the recombination of photogenerated charge carriers for higher metal loadings,

depending on the synthesis method, constitutes important disadvantages [22–24]. Non metal-doping seems to be an alternative effective method to increase the response to visible-light [25–27]. N-doped $SrTiO_3$ ($SrTiO_{3-x}N_x$) materials have been previously studied and they showed good photo reactivity and stability under both UV and visible-light irradiation [28]. In most cases hexamethylenetetramine was used as a nitrogen source for preparation methods like solid phase, mechanochemical reaction and solvothermal synthesis [29–31]. For the mechanochemical reaction, urea and ammonium carbonate have also been used as nitrogen sources in N-doped $SrTiO_3$ materials [30]. Also, S,C-doping with thiourea as sulphur source mixed with $SrTiO_3$ powder in an agate mortar [32] and N,S co–doping with thiourea as nitrogen—sulphur source by the solid state reaction method [27] have been studied the last few years. Also by the solid state reaction S-doping has been achieved with anion of sulphur [27]. With the doping sources mentioned above the specific surface area values of the as prepared catalysts were about 4–37 $m^2\ g^{-1}$ [27,29,30,32].

The use of amino acids as dopant sources have been rarely studied [33] although their ability to form stable complexes with alkaline earth and transition metals [34,35]. In addition, amino acids have been used for the development of enhanced surface area $LaFeO_3$ [36] and N-doped $SrTiO_3$ [33] perovskites. Amino acids can form complexes with Sr^{2+} and Ti^{4+} enhancing the formation of the perovskite phase while during calcination their decomposition leads to the emission of gaseous products which help the development of higher surface areas while part of the amino and/or sulphur groups remain as dopants in the matrix of the perovskite.

Based on the previous statements, the principal aims of the study are: (i) the preparation of N and N,S-doped $SrTiO_3$ photocatalysts with visible-light response and enhanced surface using amino acids (glycine and L-histidine are used as nitrogen sources and L-cysteine is used as nitrogen and sulphur sources) as doping and specific surface promoter agents; (ii) the characterization of the prepared photocatalysts by a battery of techniques in order to reveal the key-components for their photocatalytic activity and (iii) the study of their photocatalytic activity towards the degradation of organic pollutants in aqueous phase through kinetic experiments of methylene blue (MB) dye decolorization and $^{\bullet}OH$ radicals formation by fluorescence measurements.

2. Results and Discussion

2.1. Characterization of the Prepared Photocatalysts

2.1.1. XRD Analysis

Figure 1 shows the XRD patterns for all the prepared photocatalysts assigned to $SrTiO_3$ perovskite phase with a cubic symmetry (JCPDS No. 79-0176). The dominant peaks at about 32.4°, 39.9°, 46.4°, 57.8°, 67.8° and 77.2° represent the $SrTiO_3$ (1 1 0), (1 1 1), (2 0 0), (2 1 1), (2 2 0) and (3 1 0) surfaces, respectively. The experimental measurements (black line) agree with the expected results (blue line) as denoted also from the difference measurement (red line) which is linear for all samples. The sharp peaks indicate that the obtained powders are highly crystalline and free from impurities. For the catalyst with the highest doping degree, G-N-STO3, additional diffraction peaks corresponded to $SrCO_3$ phase (22.2%) were also detected and they are denoted with (▲) symbol at $2\theta = 25.81°$. For the XRD data of each sample, a Rietveld refinement was performed as reported in Reference [37]. The crystal size of the catalysts was calculated by appropriate software according to Williamson and Hall [38] type plot method and ranged from 14.2 nm for the G-N-STO3 to 35.7 nm for the G-N-STO1 (glycine dopant source; N:Sr:Ti 1:1:1 molar ratio) as shown in Table 1. The crystal size values of the N-doped with glycine photocatalysts are decreased while doping is increased as also observed by the broader crystalline peaks for G-N-STO2 (glycine dopant source; N:Sr:Ti 2:1:1 molar ratio) and G-N-STO3 samples. The refinement parameters of % crystal phase, cell parameters (a, b and c) as well as strain analysis together with R^2 are also presented in Table 1. Compared to the STO sample, the (110) diffraction peaks of the XRD pattern for the different N-doped catalysts shifted towards higher angles as a result of nitrogen incorporation into the O^{2-} sites in $SrTiO_3$ lattice. The lattice constants

(a, b, c) for the N- and N,S-doped photocatalysts are slightly higher from those of STO. This can be attributed to the expansion of lattice because of the insertion of dopant atoms. From the calculated strain analysis it is observed that G-N-STO3 has a negative strain value at −0.029. This value probably shows that higher degree of N-doping inhibits crystal growth and deforms crystal lattice.

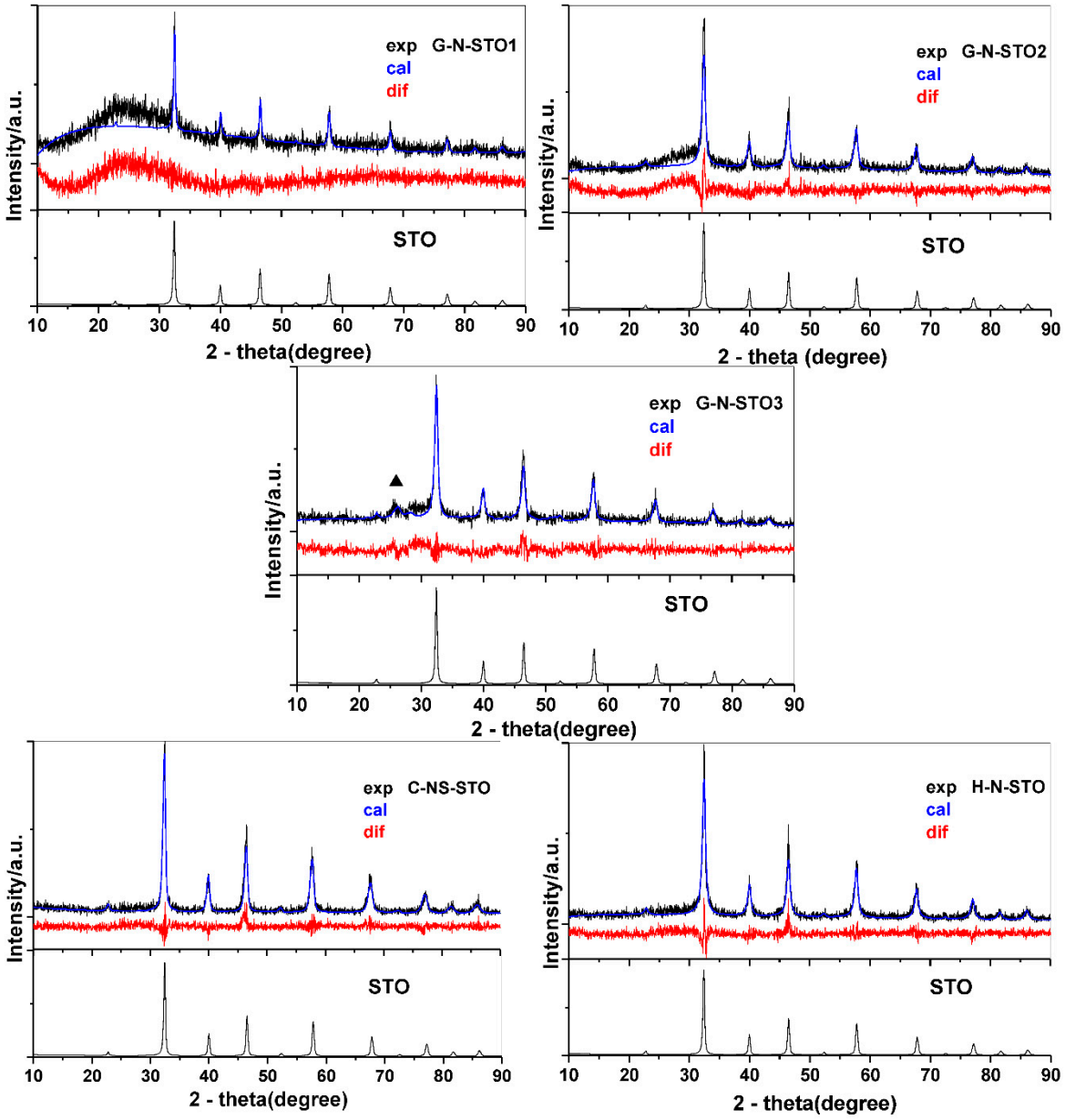

Figure 1. XRD patterns of all prepared photocatalysts (▲$SrCO_3$) in comparison with STO. The red line represents the difference plot between the experimental and the theoretical calculation.

Table 1. XRD results and Rietveld analysis of all prepared photocatalysts.

Code Name	Crystal Phase	Space Group	% Phase	a	b	c	Unit Cell Volume (A^3)	E%	*R* %	Crystal Size (nm)	% Strain	R^2
G-N-STO1	$SrTiO_3$	cubic	100	3.91048	3.91048	3.91048	59.8	31.11	70.34	35.7	0.084	0.82
G-N-STO2	$SrTiO_3$	cubic	100	3.91684	3.91684	3.91684	60.1	23.69	44.0	27.6	0.291	0.76
G-N-STO3	$SrTiO_3$	cubic	77.8	3.91899	3.91899	3.91899	60.2	22.53	30.4	14.2	−0.029	0.87
	$SrCO_3$	orthorhombic	22.2	5.03856	7.47593	5.92672	223.2	-	-	-	-	-
H-N-STO	$SrTiO_3$	cubic	100	3.91537	3.91537	3.91537	60.0	20.32	30.39	22.9	0.279	0.99
C-NS-STO	$SrTiO_3$	cubic	100	3.9194	3.9194	3.9194	60.2	19.19	27.31	25.6	0.284	0.91
STO	$SrTiO_3$	cubic	100	3.90866	3.90866	3.90866	59.7	14.79	20.62	27.5	0.016	0.93

2.1.2. Morphology—Surface Analysis of the Photocatalysts

The nitrogen adsorption—desorption isotherms for the studied catalysts are presented in Figure 2. C-NS-STO (L-cysteine dopant source: N:S:Sr:Ti 1:1:1:1) and STO photocatalysts represented non-porous materials and the isotherms belong to type–II according to IUPAC classification [39]. For G-N-STO1, G-N-STO2, G-N-STO3 and H-N-STO (L-histidine dopant source; N:Sr:Ti 1:1:1) catalysts IV(a)—type isotherms with an H2(b) hysteresis loop were observed indicating mesoporous materials according to IUPAC classification [39]. The interconnectivity of pores that are formed among inter—aggregated particles is the explanation of the H2(b) hysteresis loop formation. For G-N-STO1, G-N-STO2, G-N-STO3 photocatalysts the existence of hysteresis loop (Figure 2) is characteristic of the presence of mesopores while the peak at about 36 Å in the PSD curves is due to the presence of finer pores (micropores). The specific surface area (SSA) of all prepared photocatalysts are presented in Table 2 and ranged between 20.7 m^2/g for C-NS-STO to 89 m^2/g for the H-N-STO. It is well known that in the solution-combustion synthesis parameters such as type of fuel (different amino-acid in this case), fuel/oxidizer ratio, ignition temperature, produced flame influences the characteristics (surface area, crystallite size, agglomeration) of the produced materials [40]. For example, the rapid generation of large volume of gases during combustion reduces the possibility of sintering and creates pores between particles. On the other hand, combustion temperature can reach >1000 °C according to the produced flame enhancing the sintering [41]. It seems that the reaction in the presence of glycine is more rapid (auto-ignition 180–200 °C) in comparison with the reactions in the presence of L-cysteine (auto-ignition around 290 °C). Also, for $LaFeO_3$ perovskite synthesized by glycine process it has been reported [41] that specific surface area (SSA) values increase with the increase of glycine to nitrate ratio until a certain value while the crystal size decreases, a trend that is similar to that observed in the present study.

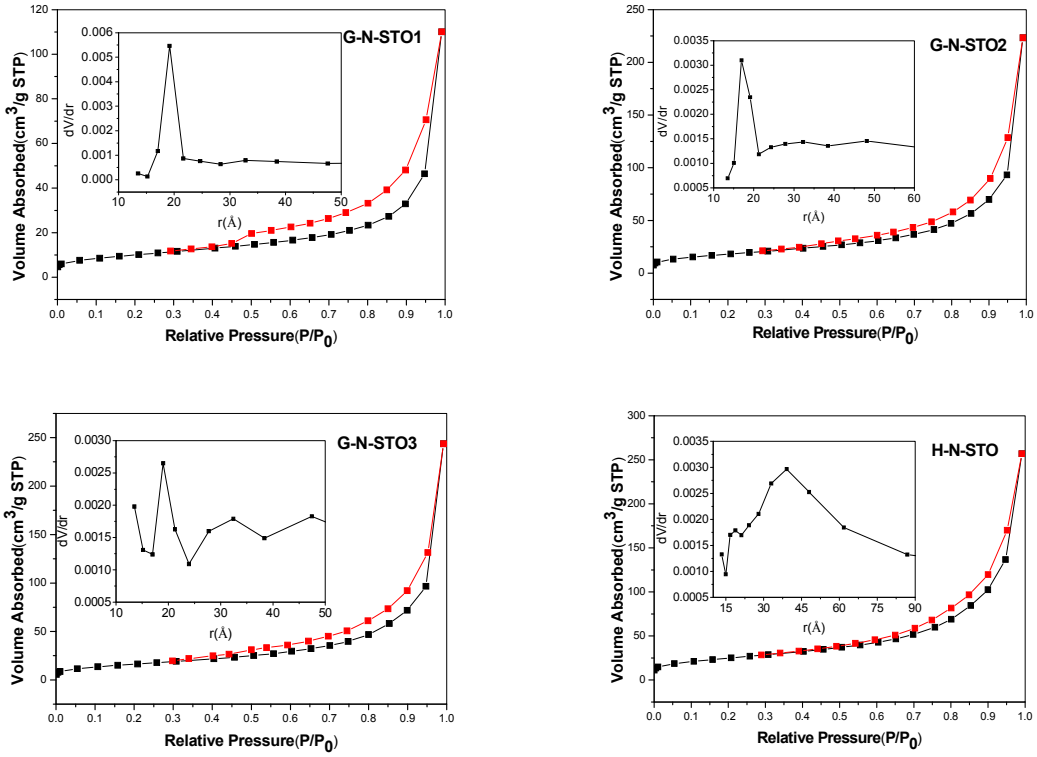

Figure 2. *Cont.*

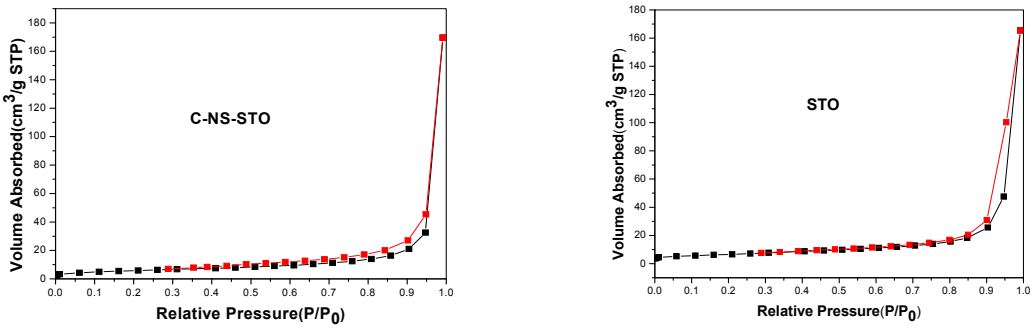

Figure 2. Adsorption—desorption isotherms and pore size distribution for all photocatalysts (G-N-STO1, G-N-STO2, G-N-STO3, H-N-STO, C-NS-STO and STO).

Table 2. Specific surface area (SSA), pore diameter (D_p), dynamic light scattering and point of zero charge results of all photocatalysts.

	SSA_{BET} (m^2 g^{-1})	D_p (Å)	DLS * (nm)	PZC	E_g (eV)
G-N-STO1	35.8	36.8	0.263	7.03	3.10
G-N-STO2	64.8	33.5	0.278	6.41	3.05
G-N-STO3	59.7	33.8	0.329	5.52	2.99
C-NS-STO	20.7	-	0.337	6.55	3.10
H-N-STO	89.0	78.0	0.273	6.38	3.13
STO	23.6	-	0.345	9.33	3.15

* Dynamic light scattering measurements (median diameter) after 10 min of sonication before the photo—irradiation experiments.

SEM images are shown in Figure 3. STO presented a structure of large uniform spherical particles with no porosity in accordance with the low SSA value determined by N_2 porosimetry. The SEM images for G-N-STO1, G-N-STO2 and G-N-STO3 show a porous structure with shapeless and irregular particles with internal cavities. The images revealed that all particles exhibited nearly identical morphologies, regardless the doping degree. On the contrary, the surface roughness increased with the nitrogen-doping degree. The images of H-N-STO present a similar but less stony structure. Finally, SEM images of C-NS-STO sample present a macroporous network with an interconnected structure into a single block of stone like a monolith.

The point of zero charge (PZC) of STO is 9.33. The N- and N,S-doping of the photocatalysts decrease the PZC. The G-N-STO1, G-N-STO2 and G-N-STO3 have PZC 6.95, 6.41 and 5.52 respectively. It is observed that while the N-doping increases in all three samples, the PZC decreases. Also, the PZC of C-NS-STO and H-N-STO is 6.55 and 6.38 respectively.

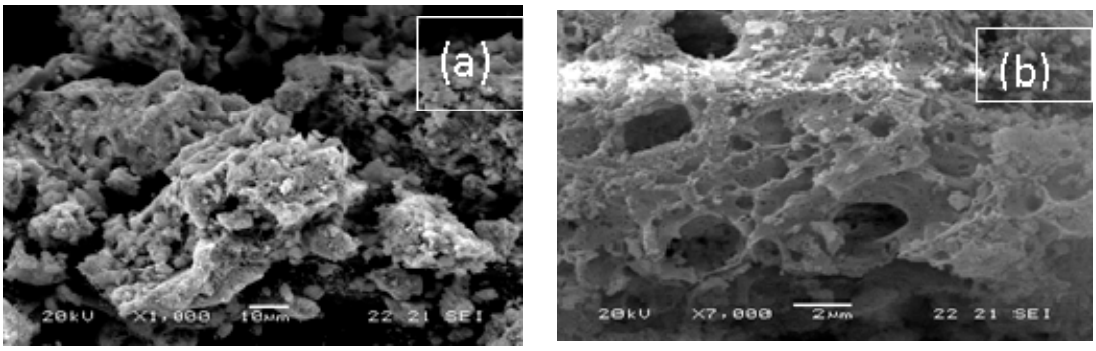

Figure 3. *Cont.*

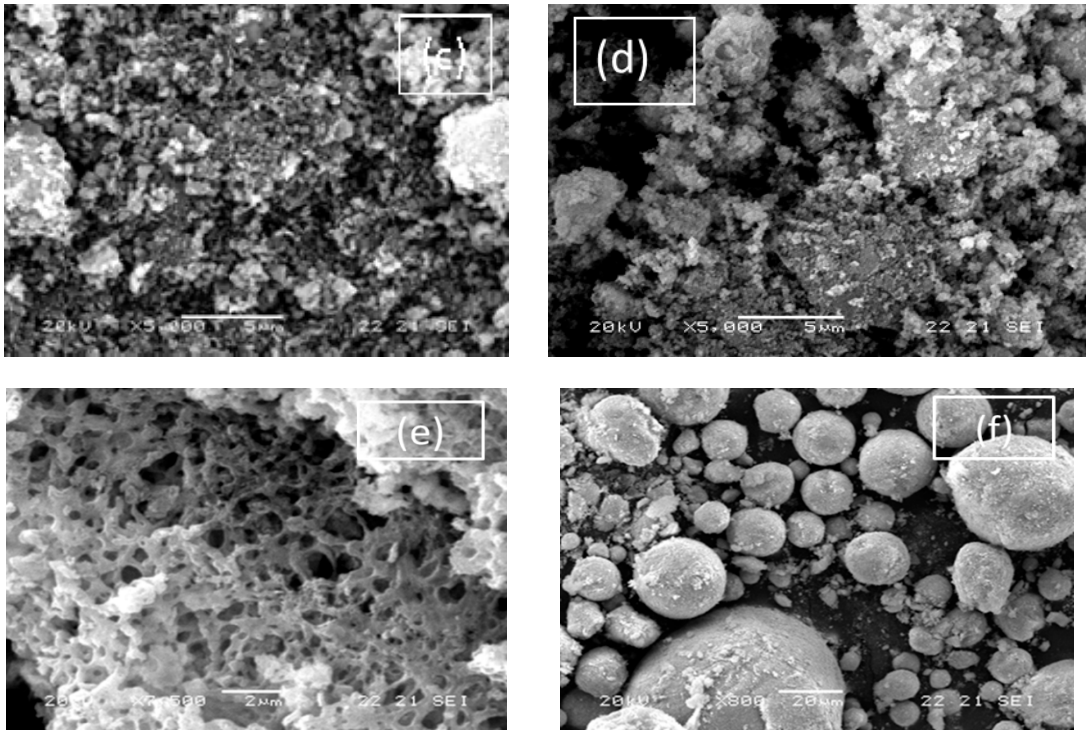

Figure 3. SEM images of all photocatalysts used in the study: (**a**) G-N-STO1; (**b**) G-N-STO2; (**c**) G-N-STO3; (**d**) H-N-STO; (**e**) C-NS-STO; (**f**) STO.

2.1.3. FT–IR Spectroscopy

The FT–IR spectra of the N, N/S—doped photocatalysts and STO are presented in Figure 4. In all samples the shoulder below 1000 cm^{-1} appears because of the $SrTiO_3$ crystal lattice vibrations [42]. Specifically, the bands around 858 and 596 cm^{-1} are caused from the stretching vibration of Sr-O and Ti-O bond, respectively [43]. Also for all samples the absorption peak around 3443–3447 cm^{-1} can be caused from the stretching vibrations of lattice hydroxyls from Ti-OH perturbed by nearby Sr atoms or by Sr-OH [42]. The band around 1637 cm^{-1} for STO is due to the bending vibration of -OH (caused from bending water) [42,44]. The absorption peak around 3443 cm^{-1} can be caused from the stretching vibrations of lattice hydroxyls from Ti-OH perturbed by nearby Sr atoms or by Sr-OH [42]. G-N-STO1, G-N-STO2 and G-N-STO3 photocatalysts have presented a characteristic peak at 1384–1386 cm^{-1} which is attributed to the stretching vibrations of interstitial N-O [45]. The intensity of this peak is proportional to the doping ration of the G-N-STO catalysts. Additionally, all three of them have a peak between 1630–1644 cm^{-1} which can be attributed to surface N-H bonds [33,46]. Also, the peak that appears at 3447 cm^{-1} corresponded to the stretching vibrations of lattice hydroxyls from Ti-OH or by Sr-OH [42,47,48]. The peaks in 2851, 2927 cm^{-1} for G-N-STO1 and in 2856, 2927 cm^{-1} for G-N-STO2 are due to CH_2 asymmetric stretching vibrations from residual organics in the material. The peak in 1261 cm^{-1} in both G-N-STO1 and G-N-STO2 is caused by C = O vibrations. In the C-NS-STO photocatalyst the small peaks at 1047 and 1263 cm^{-1} are due to the frequencies of bit—dentate S-O coordinated to Ti^{+4} [47,48]. Also the peak in 1381 cm^{-1} is attributed to the stretching vibrations of interstitial N-O [45]. The peaks in 1636 and 3440 cm^{-1} are caused from the bending vibration of –OH [48,49] and the stretching vibrations of lattice hydroxyls from Ti-OH or by Sr-OH [42,48,49] respectively. In the H-N-STO the peaks in 1637 and 1386 cm^{-1} correspond to the stretching vibrations of N-O [45] and to bending vibration of -OH [48,49], respectively. The peak in 3440 cm^{-1} is attributed to the stretching vibrations by Ti-OH or by Sr-OH [42,48,49].

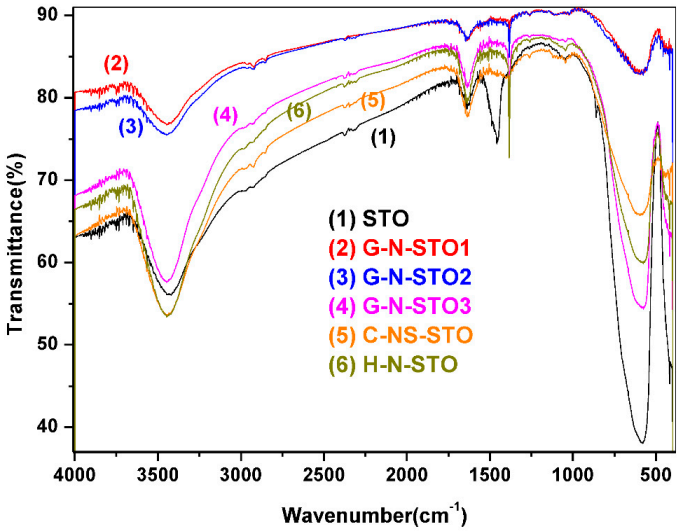

Figure 4. FT–IR spectra of the N-,N,S-doped photocatalysts and STO.

2.1.4. UV-Vis Spectra

The diffuse reflectance spectroscopy (DRS) results of all photocatalysts are presented in Figure 5a. The optical absorption edge of pure $SrTiO_3$ (STO) was about 390–395 nm as expected, so no response against visible irradiation was observed. On the other hand G-N-STO2 and G-N-STO3 were significantly red shifted to longer wavelengths into the visible light region (till 415 nm) while the absorption edges of G-N-STO1, H-N-STO and C-NS-STO presented a smaller shift (about 7 nm) in comparison to STO. The E_g values (Table 2) of all photocatalysts were calculated with the use of Kubelka—Munk plots which are presented in Figure 5b. The E_g values of the N-,N,S-doped photocatalysts had the following trend: H-N-STO > C-NS-STO,G-N-STO1 > G-N-STO2 > G-N-STO3. From this trend it can be concluded that the absorption edge of the samples prepared with glycine and among them the sample with the highest N–doping presented the greater shift to the visible light region.

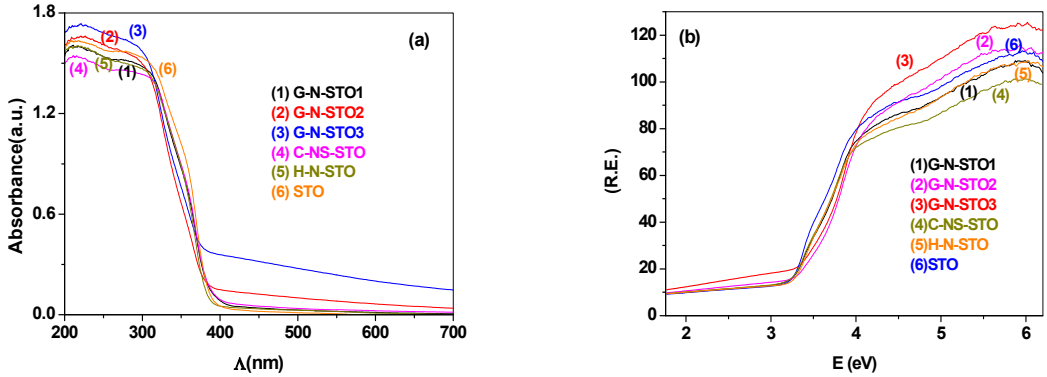

Figure 5. (**a**) DR UV—Vis spectra plots; (**b**) Kubelka—Munk plots for photocatalysts. R: absorbance, E = 1239.7/λ, energy in eV, λ = wavelength in nm.

2.1.5. Fluorescence Spectrum

The evolution of fluorescence spectra intensity of hydroxy-terephthalic acid (TAOH) for the G-N-STO3 photocatalyst at different intervals within an irradiation time framework of 120 min is displayed in Figure 6 as a characteristic example. The fluorescence spectra for the rest of photocatalysts prepared are shown in Figure S1 (Supplementary Materials). As it is shown, the fluorescence intensity increases along with time. The kinetics of $^{\bullet}$OH radicals' formation for all photocatalysts

is shown in Figure 7. The observed linear relationship between the fluorescence intensity (i.e., •OH radicals formation) and the time denoted the stability of the synthesized catalyst. The ability of the photocatalysts to generate •OH radicals followed the trend: G-N-STO3 > G-N-STO2 > G-N-STO1 > C-NS-STO > H-N-STO, STO. As a result, catalyst showed greater •OH formation compared to the catalyst prepared by cysteine and histidine while G-N-STO3, that is, the catalyst with the higher dopant content generates the largest amount of •OH. This observation can be further explained by the the formation of the $SrCO_3/SrTiO_3$ junction structure which helps reducing electron/hole pairs recombination as reported elsewhere [50].

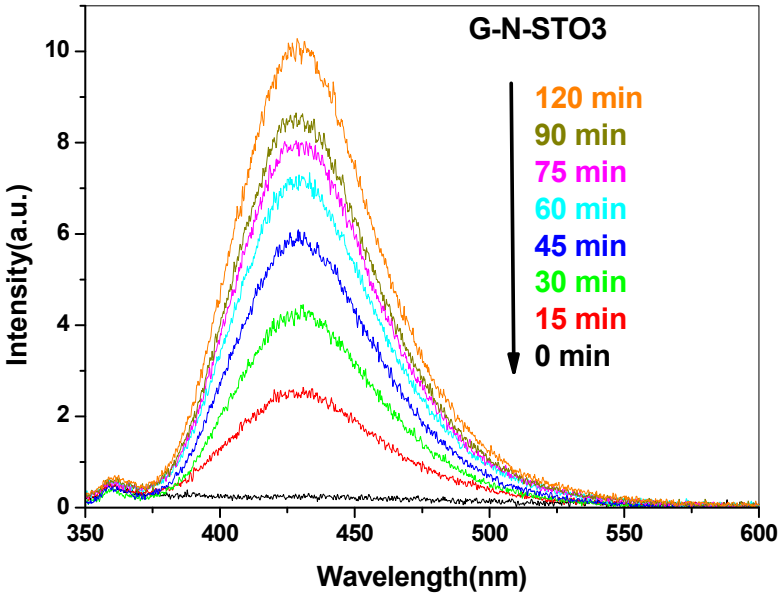

Figure 6. Fluorescence spectra after 120 min of irradiation of G-N-STO3.

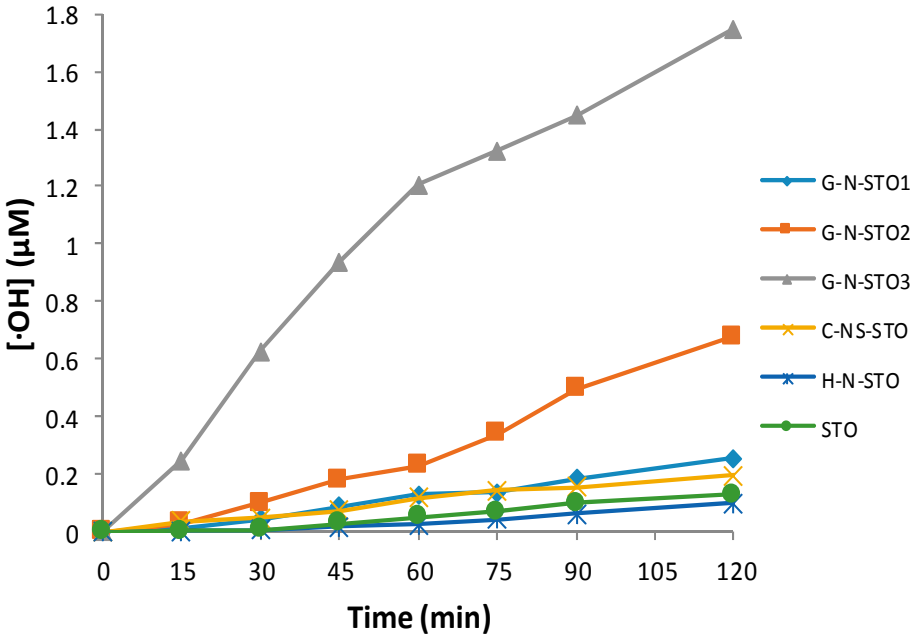

Figure 7. Formation of OH with the effect of the photocatalysts.

2.2. Photocatalytic Degradation Kinetics and Pathways of Methylene Blue (MB) under UV—Vis and Visible Light Irradiation

The photocatalytic activity of all catalysts towards the degradation of MB under UV-Vis and visible irradiation is depicted in Figures 8 and 9 respectively. The degradation for all samples followed first order kinetics. As expected, the degradation kinetics under visible light irradiation was slower than under UV–Vis (simulated solar) irradiation. The apparent rate constants (k), the corresponding correlation coefficients (R^2) and half-lives ($t_{1/2}$) of all photocatalysts are presented in Table 3. Based on the determined apparent rate constants the photocatalytic activity followed the same trend under both UV-vis and visible irradiation: G-N-STO3 > G-N-STO2 > G-N-STO1 > H-N-STO > C-NS-STO > STO. All N- and N/S-doped photocatalysts presented higher photocatalytic activity than $SrTiO_3$ while among all doped photocatalysts G-N-STO3 showed the higher photocatalytic activity. The above observations come in full agreement with the results from the characterization of the materials as previously discussed. More specifically the catalytic activity follows the same trend with the •OH production ability while G-N-STO3 was the material with the lower E_g value, that is, the higher absorption in visible region, the smallest crystallite size, that is, the lower electron—hole recombination due to more effective charge diffusion into the surface and the lowest PZC entailing the higher MB adsorption due to the attraction of negatively charged surface to the cationic dye. For the catalysts G-N-STO3, G-N-STO2 and G-N-STO1 sharing the same nitrogen source (glycine) it can be concluded that the increase of N-doping improves the photocatalytic activity. The activity follows closely the same trend as for E_g, crystal size, specific surface area, PZC and •OH production ability. In conclusion, the overall activity of the prepared catalysts is a matter of interplay of the above mentioned properties with particle size, E_g and •OH formation being the most important ones.

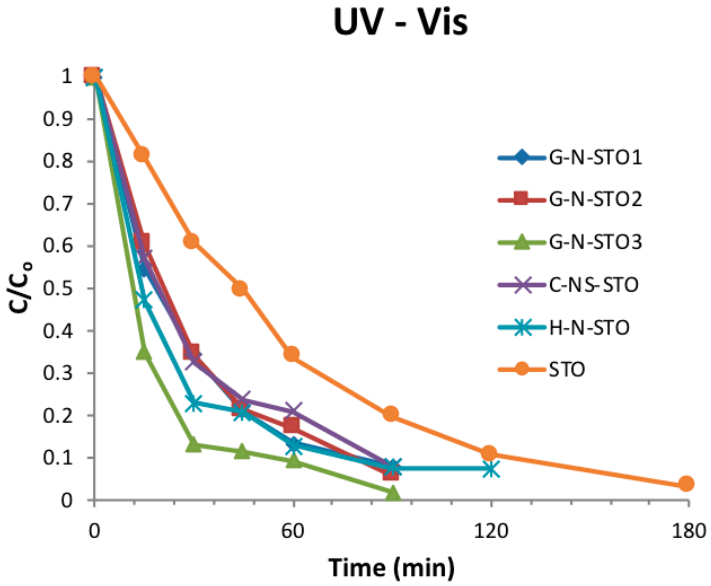

Figure 8. Degradation kinetics of MB under UV—Vis irradiation (C_{MB} = 5 mgL^{-1}, C_{cat} = 200 mgL^{-1}, I = 500 Wm^{-2}).

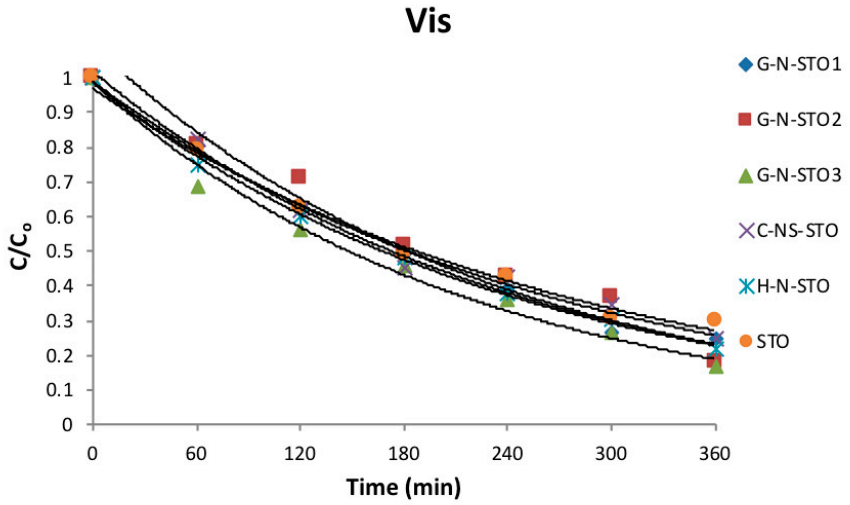

Figure 9. Degradation kinetics of MB under visible light irradiation (C_{MB} = 5 mgL^{-1}, C_{cat} = 200 mgL^{-1}, I = 500 Wm^{-2}).

Table 3. Kinetic parameters (k, $t_{1/2}$, R^2) for the photocatalytic degradation of MB in the presence of $SrTiO_3$ catalysts under simulated solar light (UV-Vis) and visible light irradiation; (C_{MB} = 5 mgL^{-1}, C_{cat} = 200 mgL^{-1}, I = 500 Wm^{-2}).

	UV-Visible Light			Visible Light		
	k (min^{-1})	$t_{1/2}$ (min)	R^2	k (min^{-1})	$t_{1/2}$ (min)	R^2
G-N-STO1	0.0283	24.5	0.9775	0.0041	169.1	0.9895
G-N-STO2	0.0306	22.6	0.9915	0.0043	161.2	0.9358
G-N-STO3	0.0399	17.4	0.9429	0.0046	150.7	0.9804
C-NS-STO	0.0268	25.9	0.9758	0.0037	187.3	0.9815
H-N-STO	0.0273	25.4	0.9346	0.0041	169.1	0.9971
STO	0.0193	35.9	0.9982	0.0035	198.0	0.9834

In Figure 10a,b the profiles of the temporal change in absorbance of MB for G-N-STO3 catalyst are presented for both UV-Vis and visible light irradiation. Based on the spectral profiles the degradation route of MB in both UV-Vis and visible light can be proposed. The characteristic absorption peaks of MB around 246, 291 and 664 nm correspond to benzene and heteropolyaromatic rings, respectively. It can be observed that the characteristic peaks decreased with time while 665 nm peak shifted towards the blue region (hypsochromic effect). Figures S2 and S3 (Supplementary Materials) presented the blue shift in MB spectra along the photocatalytic treatment in the presence of the prepared photocatalysts under UV-Vis and visible light irradiation. The blue shift in λ_{max} suggested the stepwise removal of auxochromes (methyl or methylamine) [49,51]. As a result the degradation pathway of MB can be suggested to follow consecutive N-demethylation as reported also elsewhere in the literature [52]. The electron donor properties of methyl groups facilitate the attack of $^{\bullet}$OH radicals for the demethylation pathway, which is considered to be an important step in the degradation of MB [49,51]. The intermediates can be identified based on the different absorption spectra characteristics as follows: azure B (λ_{max}: 648–655 nm), azure A (λ_{max}: 620–634 nm), azure C (λ_{max}: 608–612 nm) and thionine or phenothiazine (λ_{max}: 602 nm) [49]. Under UV-Vis light irradiation all the above mentioned intermediates are formed and after 180 min of irradiation only a small band between 246 and 291 nm was still present showing the presence of low concentrations of benzene derivatives and almost complete degradation. On the other hand, under visible light after 360 min of irradiation only azure B is formed while the bands at 246, 291 nm were only slightly decreased suggesting the much lower degree of degradation.

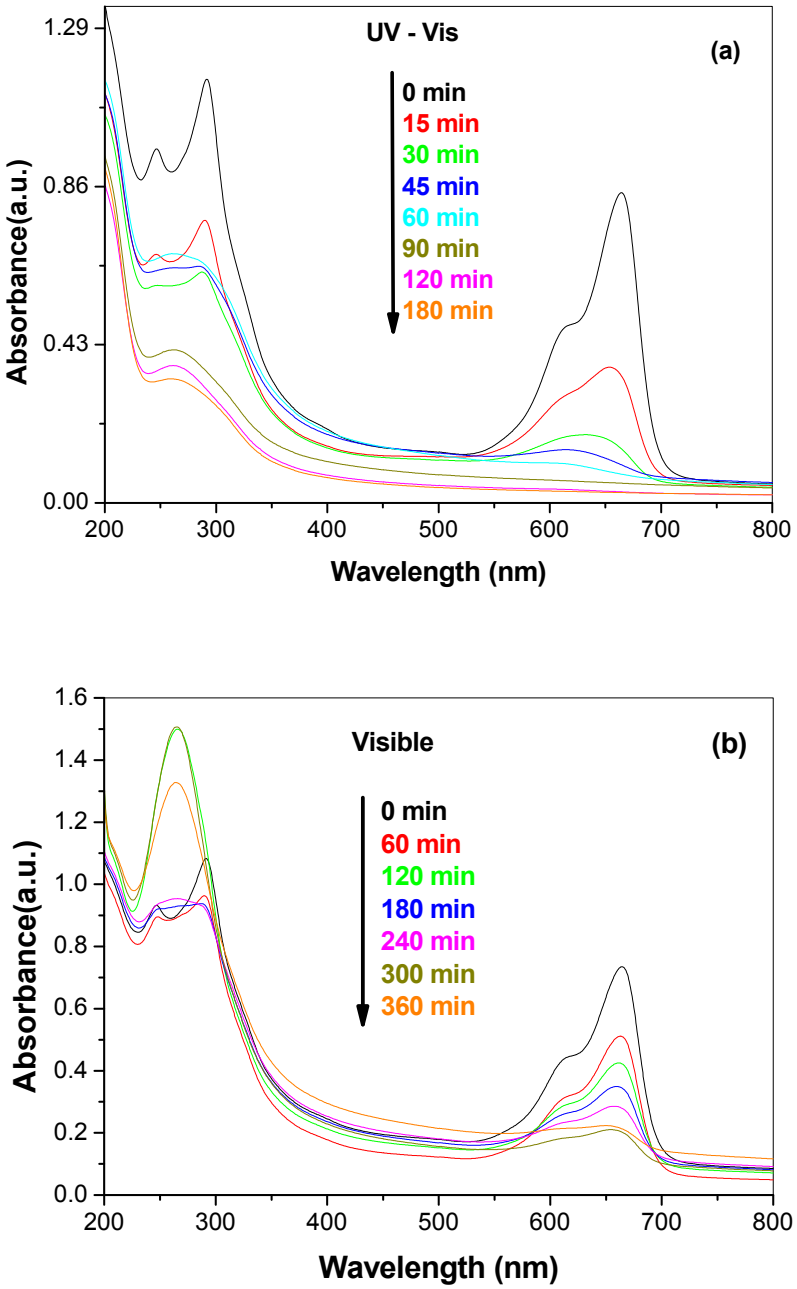

Figure 10. Temporal change of MB with irradiation time on G-N-STO3 photocatalyst under (**a**) UV-Vis; (**b**) Visible light irradiation (C_{MB} = 5mgL^{-1}, C_{cat} = 200 mgL^{-1}).

Finally, the stability of the best catalyst (G-N-STO3) for three consecutive photocatalytic cycles was also investigated. As shown in Figure 11, the catalyst presented a stable photocatalytic activity among the repeated catalytic cycles and about 95% of the initial degradation efficiency was maintained suggesting the G-N-STO3 catalyst has a good reusability. The slight decrease in the photocatalytic efficiencies could be ascribed either to a minor extent of accumulation of later stage products into the catalyst surface after the first catalytic cycle or to small losses of catalyst during the recovery procedure due to the good dispersibility into the aqueous solution.

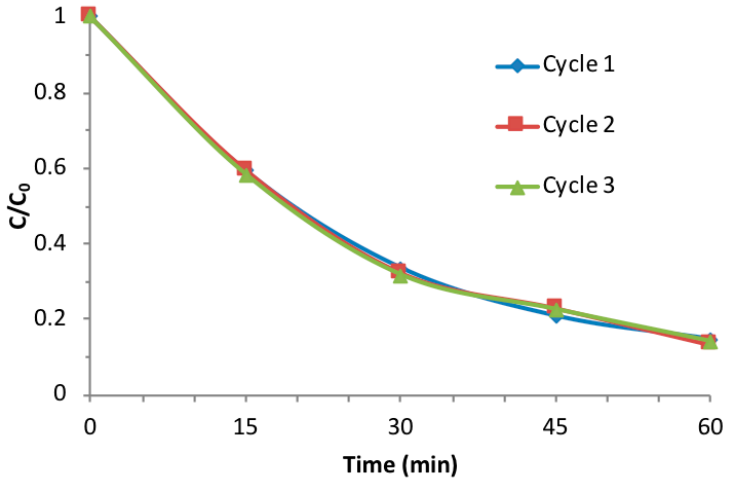

Figure 11. Stability of the G-N-STO3 catalyst upon three catalytic cycles.

3. Materials and Methods

3.1. Chemicals

Glycine (99.5%) was obtained by AppliChem (Darmstadt, Germany) and L-histidine (≥99%) and L-cysteine (97%) were purchased from Sigma-Aldrich (St. Louis, MO, USA). Strontium nitrate [$Sr(NO_3)_2$] (>99% non-hydrate) was supplied by Merck (Kenilworth, NJ, USA) and tetrabutyltitanate (TBT, $C_{16}H_{36}O_4Ti$) (97%) by Sigma-Aldrich, (St. Louis, MO, USA). Absolute ethanol (99.8%) was obtained by Acros Organics (Geel, Belgium) and glacial acetic acid (99.7%) by Panreal (Barcelona, Spain). Double distilled water was used throughout the experimental procedures of the study.

3.2. Preparation of N and N,S-Doped $SrTiO_3$ Photocatalysts

The preparation method for the N and N,S-doped $SrTiO_3$ photocatalysts was the autoignition-combustion technique of amino acids [53–55]. Amino acids are selected as doping agents because of their ability to form stable complexes with alkaline earth and transition metals [33] and serve both as a fuel and as complexant to prevent selective precipitation of precursor components before combustion, favouring the compositional homogeneity and thus the crystallization of perovskite after combustion. The selected amino acids were glycine, L-histidine and L-cysteine. In this technique 5 mL of aqueous solution containing appropriate amount of each amino acid and 10 mmol $Sr(NO_3)_2$ were added drop by drop into 40 mL ethanol solution containing 10 mmol of TBT and 2 mL glacial acetic acid under rigorous stirring, following with evaporation at 50 °C again under rigorous stirring in a fume hood. The obtained dry gel was ground and calcinated at 550 °C/2 h, with a temperature ramp of 10 °C/min [33]. The as prepared materials, except of the formation of cubic $SrTiO_3$ phase in all of them, showed the formation of small amounts of $SrCO_3$ in the N-doped photocatalysts and small amounts of both $SrCO_3$ and $SrSO_4$ in the N,S-doped photocatalysts. Also the samples G-N-STO1, G-N-STO2 and G-N-STO3 contained in small amounts a $(SrO)_2TiO_2$ phase. So, a cleaning process was made. The materials G-N-STO1 and H-N-STO were washed with 50 mL of nitric acid (HNO_3 65%, Merck) 1M heated at 70 °C and the materials G-N-STO2 and G-N-STO3 with 100 mL of nitric acid 2M heated at 70 °C [37]. In both cases after the cleaning procedure the samples were washed with distilled water. The C-NS-STO sample was washed with 100 mL 2M of both HNO_3 and potassium hydroxide (KOH, pellets 85%, Merck) [56,57] which were both heated at 70 °C and then washed with distilled water. The prepared materials had the following molar ratios and code names in parenthesis: (a) glycine dopant source: N:Sr:Ti 1:1:1 (G-N-STO1), 2:1:1 (G-N-STO2), 3:1:1 (G-N-STO3); (b) L-histidine dopant source: N:Sr:Ti 1:1:1 (H-N-STO); (c) L-cysteine dopant source: N:S:Sr:Ti 1:1:1:1 (C-NS-STO). Pure $SrTiO_3$(STO) was also used for comparison to the doped photocatalysts.

3.3. Texture Characterization of the Catalysts

Purity and crystallinity phases of the catalysts were determined by powder X-ray diffraction (XRD) using a Bruker Advance D8 XRD instrument (Billerica, MA, USA) which generates monochromated Cu K_a (λ = 1.5418 Å) radiation with a continuous scanning rate in the range of $10 < 2\theta < 90$ in steps of 0.02° and rate 0.01 °θ/s. The patterns were assigned with the use of the Joint Committee on Powder Diffraction Standards (JCPDS) database. The results were studied with Rietvield refinement by an appropriate computer program. The results are presented in Figure 1 and Table 1.

The N_2 adsorption—desorption isotherms at 77 K were obtained by porosimetry using a Quantachrome Autosorb-1 (Bounton Beach, FL, USA) instrument. Each sample (≈0.1 g) was degassed for 4h at 353 K in order to achieve the elimination of any moisture and condensed volatiles. Brauner-Emmet-Teller (BET) method at relative pressure between 0.05–0.3 was used in order to calculate the specific surface area (SSA). Adsorbed amount of nitrogen at relative pressure $P/P_0 = 0.99$ was used in order to calculate the total pore volume (V_{TOT}). The BJH method was used to determine the pore size distribution (PSD) of the photocatalysts. In Figure 2 the adsorption – desorption isotherms and PSD are shown. The SSA and the pore diameter (D_p) at the maximum of the PSD for all photocatalysts are shown in Table 2. The morphology of the photocatalysts was observed by scanning electron microscopy (SEM) by a JEOL JSM 5600 (Tokyo, Japan) instrument and characteristic images are shown in Figure 3.

Particle size measurements were made with a Shimadzu SALD-2300 (Kyoto, Japan) laser diffraction particle size analyser in dynamic light scattering (DLS) mode. Suspensions of the N and N,S-doped $SrTiO_3$photocatalysts were prepared by sonication with a Hielscher UP100H (Teltow, Germany) ultrasonic processor for 10 min. The point of zero charge (PZC) of the photocatalysts was calculated by the mass titration method as it is described in reference [58].

3.4. Fourier Transform Infrared Spectroscopic (FT–IR) Analysis

The chemical structure of all photocatalysts was recorded by using the Fourier transform infrared spectroscopic (FT–IR) analysis. The analysis was carried out with an instrument by Thermo Scientific (Nicolet iS5) (Waltham, MA, USA). Spectral grade KBr (≥99%, Sigma-Aldrich, St. Louis, MO, USA) was used as a reference. Photocatalyst materials were ground with KBr in 1:3 ratio and made into pellets using a hydraulic press. The pellet was scanned at 0.964 cm^{-1} in the range 4000–400 cm^{-1}.

3.5. UV-Vis-DRS Measurements

The absorbance spectra of the N and N,S-doped $SrTiO_3$ photocatalysts were obtained by a Shimadzu 2600 (Kyoto, Japan) spectrophotometer which was equipped with an ISR-2600 integrating sphere at room temperature with $BaSO_4$ (NacalaiTesque, extra pure reagent, Kyoto, Japan) as the reference sample in the range of 200–800 nm. The UV-Vis DRS and Kubelka-Munk plots are presented in Figure 5a,b.

3.6. Determination of •OH Radicals by Fluorescence Measurements

Terephthalic acid (TA) (98%, Sigma-Aldrich, St. Louis, MO, USA) was used as a probe in order to determine the hydroxyl radical formation rate [59]. An aqueous solution contained of NaOH (2×10^{-3} M, 99% Riedel-de Haen, Seelze, Germany) and TA (5×10^{-4} M) was prepared and then 20 mg of photocatalyst powder was suspended in the photocatalytic reactor and stirred for 30 min under UV-Vis irradiation. The irradiation conditions were the same with the conditions during the photocatalytic experiments. Aliquots of 5 mL of the suspension were taken out at different time intervals and filtered using 0.45 μm membrane filter. A fluorescence spectrophotometer (Shimadzu RF-5300PC, Kyoto, Japan) was used to measure the intensity of the fluorescence peak at 425 nm with 310 nm excitation which is attributed to 2-hydroxyterephthalic acid (TAOH) and it is known to be

proportional to the amount of $^{\bullet}$OH radicals produced. The concentration of $^{\bullet}$OH was measured by a calibration curve plotting the fluorescence intensity of standard TAOH (TCI, >98%) solutions.

3.7. Photocatalytic Experiments and Analytical Methods

The photocatalytic experiments were conducted with Suntest XLS+ apparatus (Atlas, Linsengericht, Germany) under UV-Vis irradiation (simulated solar light, $\lambda > 300$ nm). A xenon lamp (2.2 kW), jacked with special 290 nm cut-off glass filter, was the light source. During the experiments the irradiation intensity was maintained at 500 W m^{-2}. Experiments under visible light irradiation ($\lambda > 400$ nm) were performed by LED flood lamps (LG SMD, LED, 45 pcs; Seoul, Korea) 2×50 Wm^{-2}. The photocatalytic activity was tested against the degradation of methylene blue (MB).

In both UV-Vis and visible photocatalytic experiments, before the experimental procedure bega n, 200 mgL^{-1} of the photocatalysts were sonicated for 10 min in an aqueous solution. In the experiments 200 mL of MB solution were loaded in appropriate Pyrex glass reactor (250 mL) at ambient conditions (25 ± 1 °C), by water circulation in the water jacket of the reactor and air-circulation, under continuous stirring. The pH of the solution was adjusted at a value of 7.0. Before illumination the suspension was magnetically stirred for 30 min to ensure the establishment of adsorption-desorption equilibrium onto the catalyst surface. Samples of 5 mL were withdrawn regularly from the reactor and centrifuged (Thermo Scientific, HERAUS Megafuge 8, SuZhou, China; 4400 rpm) immediately for 15 min in order to separate the catalyst particles. The supernatant transparent solution was analysed by UV-vis spectroscopy (Jasco-V650; Tokyo, Japan) measuring the absorbance at the characteristic wavelength 665 nm using a calibration curve. Relative errors lower than 4.3% were obtained in all cases. For the experiments of catalyst recycling, the materials were recovered by centrifugation, dried at 373 K for 4 h then re-suspended-irradiated using the same experimental conditions.

4. Conclusions

Visible-light active N- and N,S-doped $SrTiO_3$ photocatalysts have been synthesized using amino acids as dopants source and surface area promoters. The applied preparation method leads to micro-mesoporous, mesoporous and non-porous catalysts depending on the amino acid dopant source with extended absorption edges into the visible region. The catalysts prepared using glycine showed better photocatalytic performance towards MB decolorization compared with the catalysts prepared using cysteine or L-histidine. Among glycine-derived N-doped $SrTiO_3$ the catalyst with the higher ratio ofN-dopant showed the best efficiency for the degradation of MB dye as a result of the higher surface area, the lower band gap and the smaller crystallite sizes resulting in the higher production of OH radicals and thus to faster degradation kinetics. Finally, the best catalyst showed excellent stability and recyclability maintain the initial activity after five consecutive catalytic cycles.

Supplementary Materials: The following are available online at http://www.mdpi.com/2073-4344/8/11/528/s1, Figure S1: Fluorescence spectra after 120 min of irradiation of (a) G-N-STO1, (b) G-N-STO2, (c) H-N-STO, (d) C-NS-STO, (e) STO. Figure S2: Blue shift in MB spectra during the photocatalytic degradation in the presence of the prepared photocatalysts under visible light irradiation. Figure S3: Blue shift in MB spectra during the photocatalytic degradation in the presence of the prepared photocatalysts under UV-Vis light irradiation.

Author Contributions: Conceptualization and methodology, I.K., D.P. and T.A.; Validation, P.-S.K.; Formal analysis, P.-S.K.; Investigation, Data curation, P.-S.K.; Writing—original draft preparation, P.-S.K. and I.K.; Writing—review and editing, P.-S.K., I.K., D.P. and T.A.; Supervision, T.A. and I.K.

Funding: This research received no external funding.

Conflicts of Interest: The authors declare no conflict of interest.

References

1. Grabowska, E. Selected perovskite oxides: Characterization, preparation and photocatalytic properties—A review. *Appl. Catal. B Environ.* **2016**, *186*, 97–126. [CrossRef]

2. Kanhere, P.; Chen, Z. A Review on Visible Light Active Perovskite-Based Photocatalysts. *Molecules* **2014**, *19*, 19995–20022. [CrossRef] [PubMed]
3. Tanaka, H.; Misono, M. Advances in designing perovskite catalysts. *Curr. Opin. Solid State Mater. Sci.* **2001**, *5*, 381–387. [CrossRef]
4. Bhalla, A.; Guo, R.; Roy, R. The perovskite structure—A review of its role in ceramic science and technology. *Mater. Res. Innov.* **2000**, *4*, 3–26. [CrossRef]
5. Kato, H.; Sasaki, Y.; Shirakura, N.; Kudo, A. Synthesis of highly active rhodium-doped $SrTiO_3$ powders in *Z*-scheme systems for visible-light-driven photocatalytic overall water splitting. *J. Mater. Chem. A* **2013**, *1*, 12327–12333. [CrossRef]
6. Jia, Y.; Shen, S.; Wang, D.; Wang, X.; Shi, J.; Zhang, F.; Han, H.; Li, C. Composite $Sr_2TiO_4/SrTiO_3$(La, Cr) heterojunction based photocatalyst for hydrogen production under visible light irradiation. *J. Mater. Chem. A* **2013**, *1*, 7905–7912. [CrossRef]
7. Maeda, K. Rhodium-Doped Barium Titanate Perovskite as a Stable p-Type Semiconductor Photocatalyst for Hydrogen Evolution under Visible Light. *ACS Appl. Mater. Interfaces* **2014**, *6*, 2167–2173. [CrossRef] [PubMed]
8. Alammar, T.; Hamm, I.; Wark, M.; Mudring, A.-V. Low-temperature route to metal titanate perovskite nanoparticles for photocatalytic applications. *Appl. Catal. B Environ.* **2015**, *178*, 20–28. [CrossRef]
9. Sulaeman, U.; Yin, S.; Sato, T. Solvothermal synthesis and photocatalytic properties of chromium-doped $SrTiO_3$ nanoparticles. *Appl. Catal. B Environ.* **2011**, *105*, 206–210. [CrossRef]
10. Yu, H.; Wang, J.; Yan, S.; Yu, T.; Zou, Z. Elements doping to expand the light response of $SrTiO_3$. *J. Photochem. Photobiol. A Chem.* **2014**, *275*, 65–71. [CrossRef]
11. Wang, J.; Yin, S.; Komatsu, M.; Sato, T. Lanthanum and Nitrogen Co-Doped $SrTiO_3$ Powders as Visible Light Sensitive Photocatalyst. *J. Eur. Ceram. Soc.* **2005**, *25*, 3207–3212. [CrossRef]
12. Cao, T.; Li, Y.; Wang, C.; Shao, C.; Liu, Y. A Facile In Situ Hydrothermal Method to $SrTiO_3/TiO_2$ Nanofiber Heterostructures with High Photocatalytic Activity. *Langmuir* **2011**, *27*, 2946–2952. [CrossRef] [PubMed]
13. Van Benthem, K.; Elsässer, C.; French, R. Bulk electronic structure of $SrTiO_3$: Experiment and theory. *J. Appl. Phys.* **2001**, *90*, 6156–6164. [CrossRef]
14. Sayama, K.; Mukasa, K.; Abe, R.; Abe, Y.; Arakawa, H. A new photocatalytic water splitting system under visible light irradiation mimicking a Z-scheme mechanism in photosynthesis. *J. Photochem. Photobiol. A Chem.* **2002**, *148*, 71–77. [CrossRef]
15. Jiang, Z.; Xiao, T.; Kuznetsov, V.L.; Edwards, P.P. Turning carbon dioxide into fuel. *Philos. Trans. R. Soc. Lond. A* **2010**, *368*, 3343–3364. [CrossRef] [PubMed]
16. Konta, R.; Ishii, T.; Kato, H.; Kudo, A. Photocatalytic activities of noble metal ion doped $SrTiO_3$ under visible light irradiation. *J. Phys. Chem. B* **2004**, *108*, 8992–8995. [CrossRef]
17. Zhou, X.; Shi, J.; Li, C. Effect of metal doping on electronic structure and visible light absorption of $SrTiO_3$ and $NaTaO_3$ (Metal = Mn, Fe and Co). *J. Phys. Chem. CA* **2011**, *115*, 8305–8311. [CrossRef]
18. Kato, H.; Kudo, A. Visible-Light-Response and photocatalytic activities of TiO_2 and $SrTiO_3$ photocatalysts codoped with antimony and chromium. *J. Phys. Chem. B* **2002**, *106*, 5029–5034. [CrossRef]
19. Ishii, T.; Kato, H.; Kudo, A. H_2 evolution from an aqueous methanol solution on $SrTiO_3$ photocatalysts codoped with chromium and tantalum ions under visible light irradiation. *J. Photochem. Photobiol. A Chem.* **2004**, *163*, 181–186. [CrossRef]
20. Yu, H.; Ouyang, S.; Yan, S.; Li, Z.; Yu, T.; Zou, Z. Sol-gel hydrothermal synthesis of visible-light-driven Cr-doped $SrTiO_3$ for efficient hydrogen production. *J. Mater. Chem.* **2011**, *21*, 11347–11351. [CrossRef]
21. Puangpetch, T.; Chavadej, S.; Sreethawong, T. Hydrogen production over Au-loaded mesoporous-assembled $SrTiO_3$ nanocrystal photocatalyst: Effects of molecular structure and chemical properties of hole scavengers. *Energy Convers. Manag.* **2011**, *52*, 2256–2261. [CrossRef]
22. Colon, G.; Maicu, M.; Hidalgo, M.C.; Navio, J.A. Cu-doped TiO_2 systems with improved photocatalytic activity. *Appl. Catal. B Environ.* **2006**, *67*, 41–51. [CrossRef]
23. Zhang, Z.B.; Wang, C.C.; Zakaria, R.; Ying, J.Y. Role of Particle Size in Nanocrystalline TiO_2-Based Photocatalysts. *J. Phys. Chem. B* **1998**, *102*, 10871–10878. [CrossRef]
24. Kappadan, S.; Gebreab, T.W.; Thomas, S.; Kalarikkal, N. Tetragonal $BaTiO_3$ nanoparticles: An efficient photocatalyst for the degradation of organic pollutants. *Mater. Sci. Semicond. Process.* **2016**, *51*, 42–47. [CrossRef]

25. Asahi, R.; Morikawa, T.; Ohwaki, T.; Aoki, K.; Taga, Y. Visible-Light Photocatalysis in Nitrogen-Doped Titanium Oxides. *Science* **2001**, *293*, 269–271. [CrossRef] [PubMed]
26. Liu, J.; Wang, L.; Liu, J.; Wang, T.; Qu, W.; Li, Z. DFT study on electronic structures and optical absorption properties of C, S cation-doped $SrTiO_3$. *Cent. Eur. J. Phys.* **2009**, *7*, 762–767. [CrossRef]
27. Wang, J.; Li, H.; Li, H.; Yin, S.; Sato, T. Preparation and photocatalytic activity of visible light-active sulfur and nitrogen co-doped $SrTiO_3$. *Solid State Sci.* **2009**, *11*, 182–188. [CrossRef]
28. Sulaeman, U.; Yin, S.; Sato, T. Solvothermal Synthesis and Photocatalytic Properties of Nitrogen-Doped $SrTiO_3$ nanoparticles. *J. Nanomater.* **2010**, *2010*, 32. [CrossRef]
29. Wang, J.; Yin, S.; Komatsu, M.; Zhang, Q.; Saito, F.; Sato, T. Preparation and Characterization of Nitrogen Doped $SrTiO_3$ Photocatalyst. *J. Photochem. Photobiol. A Chem.* **2004**, *165*, 149–156. [CrossRef]
30. Xu, J.; Wei, Y.; Huang, Y.; Wang, J.; Zheng, X.; Sun, Z.; Fan, L.; Wu, J. Solvothermal synthesis nitrogen doped $SrTiO_3$ with high visible light photocatalytic activity. *Ceram. Int.* **2014**, *40*, 10583–10591. [CrossRef]
31. Yan, J.H.; Zhu, Y.R.; Tang, Y.G.; Zheng, S.Q. Nitrogen-doped $SrTiO_3/TiO_2$ composite photocatalysts for hydrogen production under visible light irradiation. *J. Alloy. Compd.* **2009**, *472*, 429–433. [CrossRef]
32. Ohno, T.; Tsubota, T.; Nakamura, Y.; Sayama, K. Preparation of S, C cation-codoped $SrTiO_3$ and its photocatalytic activity under visible light. *Appl. Catal. A Gen.* **2005**, *288*, 74–79. [CrossRef]
33. Zou, F.; Jiang, Z.; Qin, X.; Zhao, Y.; Jiang, L.; Zhi, J.; Xiao, T.; Edwards, P.P. Template-free synthesis of mesoporous N-doped $SrTiO_3$ perovskite with high visible-light-driven photocatalytic activity. *Chem. Commun.* **2012**, *48*, 8514–8516. [CrossRef] [PubMed]
34. Bush, M.F.; Oomens, J.; Saykally, R.J.; Williams, E.R. Effects of Alkaline Earth Metal Ion Complexation on Amino Acid Zwitterion Stability: Results from Infrared Action Spectroscopy. *J. Am. Chem. Soc.* **2008**, *130*, 6463–6471. [CrossRef] [PubMed]
35. Strittmatter, E.F.; Lemoff, A.S.; Williams, E.R. Structure of Cationized Glycine, Gly·M^{2+} (M = Be, Mg, Ca, Sr, Ba), in the Gas Phase: Intrinsic Effect of Cation Size on Zwitterion Stability. *J. Phys. Chem. A* **2000**, *104*, 9793–9796. [CrossRef] [PubMed]
36. Margellou, A.G.; Papadas, I.T.; Petrakis, D.E.; Armatas, G.S. Development of Enhanced Surface Area $LaFeO_3$ Perovskites Using Amino Acids as Templating Agents. *Mater. Res. Bull.* **2016**, *83*, 491–501. [CrossRef]
37. Rietveld, H.M. Line profiles of neutron powder-diffraction peaks for structure refinement. *Acta Crystallogr.* **1967**, *22*, 151–152. [CrossRef]
38. Williamson, G.K.; Hall, W.H. X-ray line broadening from filed aluminium and wolfram. *Acta Metall.* **1953**, *1*, 22–31. [CrossRef]
39. Thommes, M.; Kaneko, K.; Neimark, A.V.; Olivier, J.P.; Rodriguez-Reinoso, F.; Rouquerol, J.; Sing, K.S.W. Physisorption of gases, with special reference to the evaluation of surface area and pore size distribution (IUPAC Technical Report). *Pure Appl. Chem.* **2015**, *87*, 1051–1069. [CrossRef]
40. Alves, A.; Bergmann, C.P.; Berutti, F.A. *Novel Synthesis and Characterization of Nanostructured Materials*; Springer: Berlin/Heidelberg, Germany, 2013; ISBN 978-3-642-41274-5.
41. Kondakindi, R.R.; Karan, K.; Peppley, B.A. A simple and efficient preparation of $LaFeO_3$ nanopowders by glycine-nitrate process: Effect of glycine concentration. *Ceram. Int.* **2012**, *38*, 449–456. [CrossRef]
42. Jia, A.; Liang, X.; Su, Z.; Zhu, T.; Liu, S. Synthesis and the effect of calcination temperature on the physical-chemical properties and photocatalytic activities of Ni, La codoped $SrTiO_3$. *J. Hazard. Mater.* **2010**, *178*, 233–242. [CrossRef] [PubMed]
43. Wu, Z.; Zhang, Y.; Wang, X.; Zou, Z. Ag@$SrTiO_3$ nanocomposite for super photocatalytic degradation of organic dye and catalytic reduction of 4-nitrophenol. *New J. Chem.* **2017**, *41*, 5678–5687. [CrossRef]
44. Grabowska, E.; Marchelek, M.; Klimczuk, T.; Lisowski, W.; Zaleska-Medynska, A. $TiO_2/SrTiO_3$ and $SrTiO_3$ microspheres decorated with Rh, Ru or Pt nanoparticles: Highly UV-vis responsible photoactivity and mechanism. *J. Catal.* **2017**, *350*, 159–173. [CrossRef]
45. Smidt, E.; Böhm, K.; Schwanninger, M. *The Application of FT-IR Spectroscopy in Waste Management, Fourier Transforms—New Analytical Approaches and FTIR Strategies*; Nikolic, G., Ed.; InTech: London, UK, 2011; ISBN 978-953-307-232-6.
46. Wang, J.W.; Zhu, W.; Zhang, Y.Q.; Liu, S.X. An Efficient Two-Step Technique for Nitrogen-Doped Titanium Dioxide Synthesizing: Visible-Light-Induced Photodecomposition of Methylene Blue. *J. Phys. Chem. C* **2007**, *111*, 1010–1014. [CrossRef]

47. Ramandi, S.; Entezari, M.H.; Ghows, N. Sono-synthesis of solar light responsive S-N-C-tri doped TiO_2 photo-catalyst under optimized conditions for degradation and mineralization of Diclofenac. *Ultrason. Sonochem.* **2017**, *38*, 234–245. [CrossRef] [PubMed]
48. Tian, G.H.; Pan, K.; Fu, H.G.; Jing, L.Q.; Zhou, W. Enhanced photocatalytic activity of S-doped TiO_2-ZrO_2 nanoparticles under visible-light irradiation. *J. Hazard. Mater.* **2009**, *166*, 939–944. [CrossRef] [PubMed]
49. Gurulakshmi, M.; Selvaraj, M.; Selvamani, A.; Vijayan, P.; Sasi Rekha, N.R.; Shanthi, K. Enhanced visible-light photocatalytic activity of V_2O_5/S-TiO_2 nanocomposites. *Appl. Catal. A Gen.* **2012**, *449*, 31–46. [CrossRef]
50. Pan, X.; Chen, X.; Yi, Z. Photocatalytic oxidation of methane over $SrCO_3$ decorated $SrTiO_3$ nanocatalysts via a synergistic effect. *Phys. Chem.* **2016**, *18*, 31400–31409. [CrossRef] [PubMed]
51. Yang, C.; Dong, W.; Cui, G.; Zhao, Y.; Shi, X.; Xia, X.; Tang, B.; Wang, W. Highly efficient photocatalytic degradation of methylene blue by P2ABSA-modified TiO_2nanocomposite due to the photosensitization synergetic effect of TiO_2 and P2ABSA. *RSC Adv.* **2017**, *7*, 23699–23708. [CrossRef]
52. Zhang, T.; Oyama, T.; Aoshima, A.; Hidaka, H.; Zhao, J.; Serpone, N. Photooxidative *N*-demethylation of methylene blue in aqueous TiO_2 dispersions under UV irradiation. *J. Photochem Photobiol. A Chem.* **2001**, *140*, 163–172. [CrossRef]
53. Faye, J.; Baylet, A.; Trentesaux, M.; Royer, S.; Dumeignil, F.; Duprez, D.; Valange, S.; Tatibouët, J.-M. Influence of lanthanum stoichiometry in $La_{1-x}FeO_{3-\delta}$ perovskites on their structure and catalytic performance in CH_4 total oxidation. *Appl. Catal. B Environ.* **2012**, *126*, 134–143. [CrossRef]
54. Liu, B.; Zhang, Y. $Ba_{0.5}Sr_{0.5}Co_{0.8}Fe_{0.2}O_3$ nanopowders prepared by glycine-nitrate process for solid oxide fuel cell cathode. *J. Alloys Compd.* **2008**, *453*, 418–422.
55. Varma, A.; Mukasyan, A.S.; Rogachev, A.S.; Manukyan, K.V. Solution combustion synthesis of nanoscale materials. *Chem. Rev.* **2016**, *116*, 14493–14586. [CrossRef] [PubMed]
56. Klaytae, T.; Panthong, P.; Thountom, S. Microstructure and dielectric properties of ST ceramics prepared by the sol-gel combustion technique with chitosan addition. *Ceram. Int.* **2013**, *39*, S405–S408. [CrossRef]
57. Rangel-Hernandez, Y.M.; Rendσn-Angelesa, J.C.; Matamoros-Veloza, Z.; Pech-Canul, M.I.; Diaz-de la Torre, S.; Yanagisawa, K. One-step synthesis of fine $SrTiO_3$ particles using $SrSO_4$ ore under alkaline hydrothermal conditions. *Chem. Eng. J.* **2009**, *155*, 483–492. [CrossRef]
58. Bourikas, K.; Vakros, J.; Kordulis, C.; Lycourghiotis, A. Potentiometric Mass Titrations: Experimental and Theoretical Establishment of a New Technique for Determining the Point of Zero Charge (PZC) of Metal (Hydr) Oxides. *J. Phys. Chem. B* **2003**, *107*, 9441–9451. [CrossRef]
59. Ishibashi, K.-I.; Fujishima, A.; Watanabe, T.; Hashimoto, K. Quantum yields of active oxidative species formed on TiO_2 photocatalyst. *J. Photochem. Photobiol. A* **2000**, *134*, 139–142. [CrossRef]